STRUCTURAL BIOLOGY

ISSN: 2059-7983
journals.iucr.org/d

Structure of a hydrophobic leucinostatin derivative determined by host lattice display

Cedric Kiss, Flavio M. Gall, Birgit Dreier, Michael Adams, Rainer Riedl, Andreas Plückthun and Peer R. E. Mittl

Acta Cryst. (2022). D**78**, 1439–1450

STRUCTURAL BIOLOGY

ISSN 2059-7983

Structure of a hydrophobic leucinostatin derivative determined by host lattice display

Cedric Kiss,[a] Flavio M. Gall,[b]‡ Birgit Dreier,[a] Michael Adams,[c] Rainer Riedl,[b] Andreas Plückthun[a]* and Peer R. E. Mittl[a]*

[a]Department of Biochemistry, University of Zürich, Winterthurerstrasse 190, 8057 Zürich, Switzerland, [b]Institute of Chemistry and Biotechnology, Competence Center for Drug discovery, ZHAW Zurich University of Applied Science, Einsiedlerstrasse 31, 8820 Wädenswil, Switzerland, and [c]Bacoba AG, Elisabethenstrasse 15, 4051 Basel, Switzerland. *Correspondence e-mail: plueckthun@bioc.uzh.ch, mittl@bioc.uzh.ch

Received 21 July 2022
Accepted 10 November 2022

Edited by M. Rudolph, F. Hoffmann-La Roche Ltd, Switzerland

‡ Current address: Welmedis GmbH, Schönenbergstrasse 12, 8820 Wädenswil, Switzerland.

Keywords: crystal engineering; host lattice display; leucinostatins.

PDB references: EngBF_L1_E4_v1–ZHAWOC6027, 8a19; EngBF_L1_F11_v1–ZHAWOC6027, 8a1a

Supporting information: this article has supporting information at journals.iucr.org/d

Peptides comprising many hydrophobic amino acids are almost insoluble under physiological buffer conditions, which complicates their structural analysis. To investigate the three-dimensional structure of the hydrophobic leucinostatin derivative ZHAWOC6027, the previously developed host lattice display technology was applied. Two designed ankyrin-repeat proteins (DARPins) recognizing a biotinylated ZHAWOC6027 derivative were selected from a diverse library by ribosome display under aqueous buffer conditions. ZHAWOC6027 was immobilized by means of the DARPin in the host lattice and the structure of the complex was determined by X-ray diffraction. ZHAWOC6027 adopts a distorted α-helical conformation. Comparison with the structures of related compounds that have been determined in organic solvents reveals elevated flexibility of the termini, which might be functionally important.

1. Introduction

Leucinostatins represent a family of lipopeptides that were originally isolated from the culture broth of fungi and were identified because of their cytotoxicity to HeLa cells and bacteria. The first such lipopeptide, which was later shown to be a mixture of several compounds, was described in 1973 as 'leucinostatin' because its main component was leucine (Arai *et al.*, 1973). In early studies using mass spectrometry and NMR it was shown that leucinostatin comprised a central nonomeric peptide, where the N- and C-termini were blocked by amide bonds to a short unsaturated fatty acid and an alkyldiamine, respectively (Mori *et al.*, 1983). The central nonomeric peptide is composed of leucine and nonproteinogenic amino acids such as β-hydroxyleucine (HyLeu), β-alanine (βAla), α-aminoisobutyric acid (Aib), 4-methyl-L-proline (MePro) and (2*S*,4*S*,6*S*)-2-amino-6-hydroxy-4-methyl-8-oxodecanoic acid (AHMOD). The initially reported leucinostatin was a mixture of leucinostatin A and leucinostatin B, which differ in the composition of the C-terminal alkyldiamine (Fig. 1*a*). Just recently, the sequence of leucinostatin A was confirmed by total chemical synthesis (Watanabe *et al.*, 2021). In nature, leucinostatins have been isolated from the fungi *Paecilomyces marquandii*, *Penicillium lilacinum* and *Acremonium* sp. (Arai *et al.*, 1973; Radios *et al.*, 1987; Strobel *et al.*, 1997). The biosynthesis of leucinostatins in *P. lilacinum* and *Tolypocladium ophioglossoides* requires the concerted action of 20 gene products, including the nonribosomal peptide synthetase LcsA (Wang *et al.*, 2016).

Leucinostatins A and B are among the most toxic mycotoxins in rodents, with similar potencies to the well known

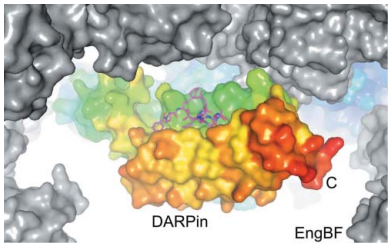

aflatoxins. The minimal concentration of leucinostatins A and B for inhibition of the proliferation of pathogenic microorganisms is in the range 1–100 µg ml^{-1} and some pathogens, such as *Plasmodium falciparum* and *Trypanosoma brucei*, are particularly susceptible. The oral LD_{50} doses in mice for leucinostatins A and B are 5.4 and 6.3 mg kg^{-1}, respectively (Fukushima *et al.*, 1983; Otoguro *et al.*, 2003). The cytotoxicity of leucinostatins A and B is attributed to their ability to inhibit ATP synthesis in mitochondria as well as various phosphorylation pathways (Fukushima *et al.*, 1983). At concentrations below 300 n*M*, leucinostatins A and B have been reported to inhibit phosphoryl transfer by binding to the F_o subunit of ATPase from rat liver mitochondria (Shima *et al.*, 1990). Alanine-scanning and truncation studies revealed that the central nonomeric peptide, in particular the hydroxyleucine and the second N-terminal leucine, are crucial for cytotoxic activity (Abe *et al.*, 2018). A comprehensive structure–activity study using *T. brucei* as a model organism revealed that destabilization of the inner mitochondrial membrane, which explains the antiprotozoal activity, can also be obtained with the simplified compound ZHAWOC6027 (Brand *et al.*, 2021; Fig. 1*b*).

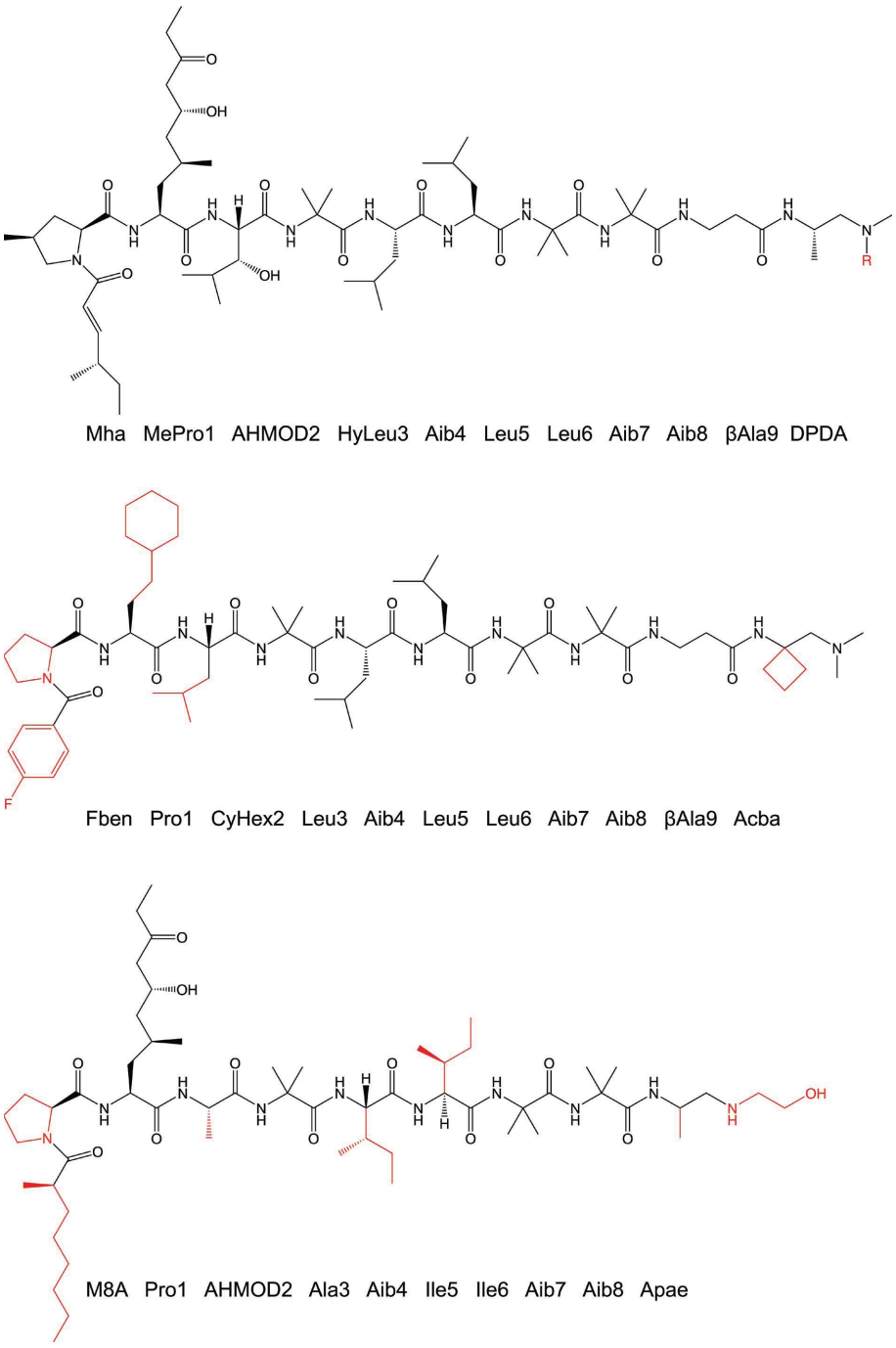

Figure 1
Formulas and sequences of (*a*) leucinostatin A (R = CH_3) and leucinostatin B (R = H), (*b*) ZHAWOC6027 and (*c*) helioferin A. Structural motifs that differ from leucinostatin A are shown in red. Amino acids are numbered and abbreviated as follows: Mha, (4*S*,2*E*)-4-methylhex-2-enoic acid; MePro, 4-methyl-L-proline; AHMOD, (2*S*,4*S*,6*S*)-2-amino-6-hydroxy-4-methyl-8-oxodecanoic acid; HyLeu, β-hydroxyleucine; Aib, aminoisobutyric acid; βAla, 3-aminopropionic acid; DPDA, N^1,N^1-dimethylpropane-1,2-diamine; Fben, *p*-fluorobenzoic acid; CyHex, (*S*)-2-amino-4-cyclohexylbutanoic acid; Acba, 1-[(dimethylamino)methyl]cyclobutan-1-amine; M8A, (2*R*)-2-methyl-*n*-1-octanoic acid; Apae, 2-(2′-aminopropyl)aminoethanol.

The crystal structure of the leucinostatin-related peptide helioferin A (Fig. 1*c*) has been determined and refined at 0.9 Å resolution (Gessmann *et al.*, 2018). Helioferin A crystals were obtained from a mixture of ethanol and acetonitrile. Since we were interested in the structure of the leucinostatin derivative ZHAWOC6027 under aqueous conditions, we avoided crystallization from organic solvents. Instead, we applied the recently established host lattice display method, a method that allows the structure of ZHAWOC6027 to be studied under predefined crystallization conditions (Ernst *et al.*, 2019).

In host lattice display the molecule of interest is displayed to the X-ray beam in a regular assembly by means of an engineered host lattice. Early attempts to support crystallization by rational crystal lattice engineering were pioneered almost three decades ago (Lawson *et al.*, 1991; Mittl *et al.*, 1994). The first practical implementations to overcome the time-consuming screening for crystallization conditions came from small-molecule crystallography (Inokuma *et al.*, 2013; Fujita *et al.*, 2012). The host–guest approach was adapted to macromolecular crystallography by the rational engineering of porous protein crystal lattices, such as

crystals of a putative periplasmic protein from *Campylobacter jejuni* (Huber *et al.*, 2018), an R1Bm endonuclease domain from *Bombyx mori* (Maita, 2018) and hemocyanin (Hashimoto *et al.*, 2019). Host–guest approaches suffer from two major limitations: (i) the crystallization conditions of the host lattice need to be independent of the guest and (ii) there is the requirement for a unique orientation of all guest molecules in the crystal relative to each other. If the orientation of the guest molecule is randomly distributed in the host lattice then clear electron density cannot be observed. Different host–guest approaches in protein crystallography have recently been reviewed (Ward & Snow, 2020).

Ernst *et al.* (2019) used the endo-α-*N*-acetylgalactosaminidase from *Bifidobacterium longum* (EngBF) to generate a host lattice (Suzuki *et al.*, 2009) and fused the N-terminus of a designed ankyrin-repeat protein (DARPin) to the C-terminus of EngBF by means of a rigid helical linker to obtain a unique incorporation of the target. The design of the helical linker together with additional disulfide bridges orient the DARPin paratope towards the solvent in the host lattice. The experimental workflow and the EngBF-DARPin fusion are shown in Figs. 2(*a*) and 2(*b*). Two different designs were generated. The L1 design offers lower *B* factors but less space for the target (Fig. 2*c*) compared with the L2 design, which theoretically would be able to host globular proteins (Ernst *et al.*, 2019).

To determine the structure of ZHAWOC6027 under native-like conditions we selected DARPins against biotinylated ZHAWOC6027 under physiological conditions and fused these DARPins to EngBF in the L1 format. The EngBF-DARPin–ZHAWOC6027 complex was subsequently crystallized under the established conditions for EngBF and the

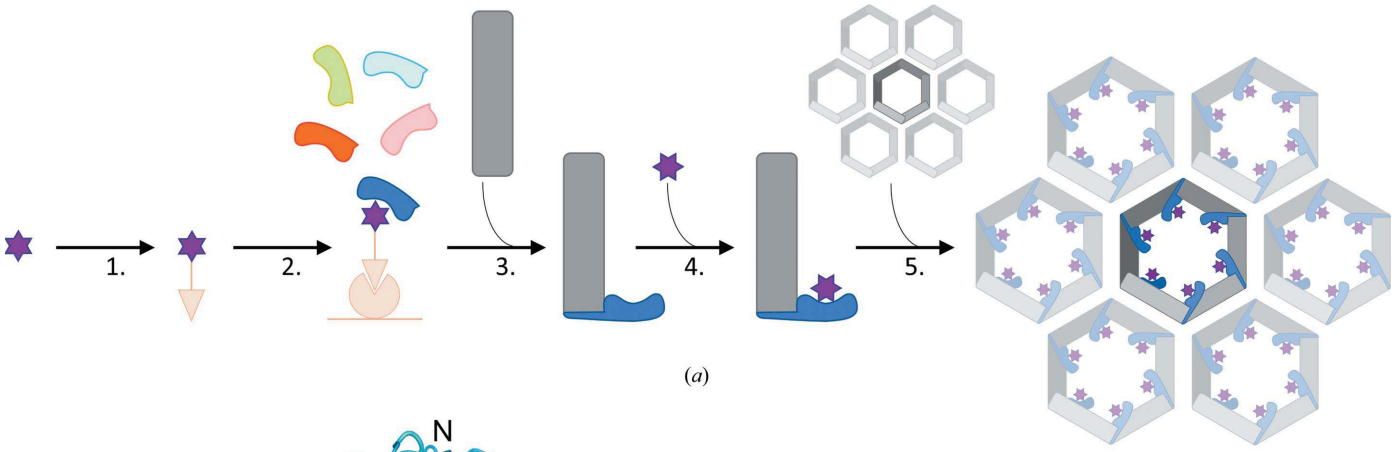

(*a*)

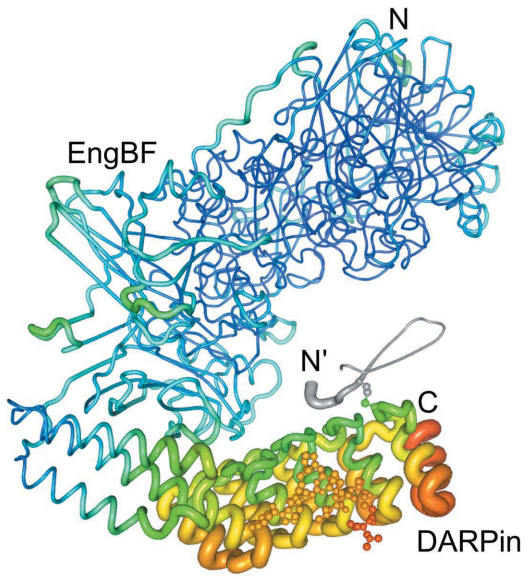

(*b*)

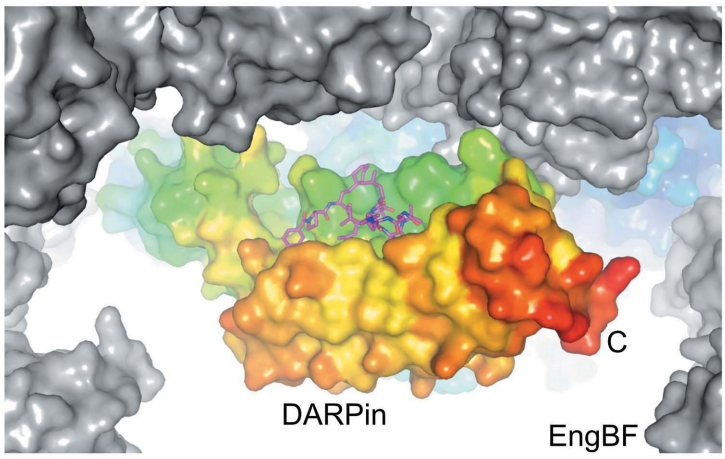

(*c*)

Figure 2
Host lattice display. (*a*) Schematic workflow of the method. 1. The target (magenta star) is biotinylated. 2. DARPin binders are selected by ribosome display on NeutrAvidin-coated plates or beads; here, the blue DARPin is identified as a high-affinity and specific binder. 3. Tight-binding DARPins (blue object) are fused to EngBF (gray box) by means of a rigid helix. 4. Formation of the EngBF-DARPin–target complex. 5. Crystallization under the established conditions for EngBF (Suzuki *et al.*, 2009). (*b*) EngBF-DARPin fusion in complex with the target molecule. EngBF_L1_E4_v1 is shown as a tube and the target ZHAWOC6027 in ball-and-stick representation colored according to *B* factor. The N-terminus of the symmetry-related complex is shown in gray and the disulfide bridge that locks the DARPin C-terminus to the symmetry-related N-terminus is also depicted in ball-and-stick representation. The N-and C-termini and the EngBF and DARPin domains are labeled. (*c*) Crystal lattice of EngBF_L1_E4_v1 viewed approximately along the 6_5 screw axis. EngBF_L1_E4_v1 is shown as a molecular surface and colored according to *B* factor, ZHAWOC6027 is shown as sticks with C atoms in magenta and symmetry-related EngBF molecules are shown as gray surfaces.

structure of ZHAWOC6027 was determined by difference Fourier methods.

2. Materials and methods

2.1. Synthesis of biotinylated ZHAWOC6027

For the selection of DARPins, a biotinylated derivative of ZHAWOC6027 was prepared by microwave-assisted solid-phase peptide synthesis (Supplementary Section S1). Solid-phase synthesis started at the C-terminus of the nonameric peptide with the Fmoc-β-Ala Wang resin and progressed towards the N-terminus using the Fmoc solid-phase technique as described in Brand *et al.* (2021). In order to attach the biotin moiety to the peptide, the N-terminal *p*-fluorobenzoic acid moiety of ZHAWOC6027 was replaced by 4-aminomethylbenzoic acid, which offers an amine group for coupling with the PEGylated biotin moiety. Finally, the biotinylated peptide was cleaved from the resin and the free carboxylic acid was amidated with 1-[(dimethylamino)methyl]cyclobutan-1-amine (Acba; Supplementary Fig. S1). The structural identity of the biotinylated peptide (ZHAWOC8403) was confirmed by mass spectrometry and ^{1}H-NMR.

2.2. Selection of DARPins against ZHAWOC6027

DARPins recognizing biotinylated ZHAWOC6027 were generated by immobilizing ZHAWOC8403 on either MyOne T1 streptavidin-coated beads (Thermo Fisher Scientific) or Sera-Mag NeutrAvidin-coated beads (Cytiva). Ribosome display selection of DARPins was performed essentially as described previously (Dreier & Plückthun, 2012; Plückthun, 2012, 2015) using a semi-automated KingFisher Flex MTP 96-well platform. In order to enrich binders with high affinity, selections were performed over three rounds with decreasing amounts of immobilized ZHAWOC8403 (250, 125 and 5 pmol) and off-rate selection during the third round, using nonbiotinylated ZHAWOC6027 as a competitor in a 1000-fold excess. This was followed by a final recovery round (50 pmol immobilized ZHAWOC8403) without competitor. During rounds 1–4 the plates were washed five times with WBT buffer (150 m*M* sodium chloride, 50 m*M* Tris acetate, 50 m*M* magnesium acetate, 0.05% Tween 20, pH 7.5) for 2, 5, 20 and 15 min, respectively. The enriched DNA pool was cloned into a bacterial pQIq-based expression vector that allows expression of the binders with an N-terminal MRGSH$_6$ tag and a C-terminal FLAG tag. After transformation of *Escherichia coli* XL1-Blue cells (Stratagene), 190 single DARPin clones were expressed in MTP 96-well plates (2YT medium supplemented with 100 mg ml^{-1} ampicillin and 1% glucose). Cultures were grown for 4 h after induction with 1 m*M* IPTG at 37°C. After centrifugation the cell pellet was lysed directly using B-PER cell-lysis buffer containing freshly added lysozyme and nuclease (ThermoFisher Scientific).

The crude bacterial cell extract of single DARPin clones was subsequently used in a high-throughput ELISA screen in which the binding of the DARPin was compared in the presence and the absence of the target peptide. Briefly, ZHAWOC8403 was immobilized on a NeutrAvidin-coated MTP384 plate. Binding was analyzed using a mouse monoclonal anti-FLAG-M2 antibody (Sigma, catalogue No. F3165) and a goat anti-mouse antibody coupled to alkaline phosphatase as a secondary antibody (Sigma, catalogue No. A3562). Target-specific binding of DARPins was analyzed by following the hydrolysis of *para*-nitrophenylphosphate at 405 nm in an ELISA plate reader (BioTek).

Successful binders were sequenced and the DARPins were obtained by small-scale expression in MTP 96 deep-well plates and purified using an MTP 96-well IMAC column (HisPur Cobalt plates, ThermoFisher Scientific). The composition of the final elution buffer was 300 m*M* sodium chloride, 50 m*M* sodium phosphate, 250 m*M* imidazole pH 7.4. From the initial 32 hits 25 single clones were successfully sequenced and purified. To assess the aggregation behavior, IMAC-purified DARPins, normalized to a concentration of 10 μ*M*, were analyzed on a Superdex 75 5/150 gel-filtration column (GE Healthcare) connected to an ÄKTA pure Micro system (GE Healthcare) using phosphate-buffered saline (PBS) as the running buffer. Chromatograms were recorded by following the absorption at a wavelength of 280 nm. The molecular weight was estimated using β-amylase (200 kDa), bovine serum albumin (66 kDa), carbonic anhydrase (29 kDa) and cytochrome *c* (12.4 kDa) as molecular-mass standards. Finally, two anti-ZHAWOC6027 DARPins designated 1016-2502-E4 and 1016-2502-F11 (abbreviated E4 and F11 in the following sections) were identified.

2.3. Cloning of EngBF-DARPin fusion proteins

DARPins E4 and F11 were cloned into the plasmid pQIq_sfGFP_EngBF_L1_DARPin_G10_His (Ernst *et al.*, 2019), which is a derivative of the pQIq vector (a lacI^q-encoding derivative of pQE30; Qiagen, Hilden, Germany) with N-terminal sfGFP and C-terminal His$_6$ tags. Both tags are fused to the EngBF construct via HRV C3 protease cleavage sites. However, E4 and F11 belong to the N2C DARPin lineage with two internal repeats, whereas DARPin G10 contains three internal repeats. The amino-acid sequences of E4 and F11 were grafted into the G10 sequence and back-translated to DNA. The DNA with the grafted sequence was synthesized at Twist Biosciences (San Francisco, USA) with HindIII/BglII restriction sites to allow in-frame fusion with the EngBF_L1 and His$_6$-tag sequences.

2.4. Expression and purification of EngBF-DARPin fusion proteins

sfGFP-3C-EngBF-DARPin-3C-His$_6$ constructs were expressed as described in Ernst *et al.* (2019). Briefly, *E. coli* BL21 Gold competent cells were transformed with the plasmids (Agilent), plated on agar plates and single colonies were grown in 5 ml 2×YT medium (supplemented with 100 μg ml^{-1} ampicillin and 1% glucose) overnight at 37°C (with orbital shaking at 240 rev min^{-1}). For expression, 200 ml TB medium (supplemented with 100 μg ml^{-1} ampicillin and 1% glucose) was inoculated with the overnight culture and incubated at 37°C with constant agitation (190 rev min^{-1}, 25 mm rotor

radius) until the OD_{600} reached 0.1. The expression temperature was reduced to 25°C for 30 min prior to induction with isopropyl β-D-1-thiogalactopyranoside at a final concentration of 0.5 m*M* (OD_{600} between 0.6 and 0.8). The expression temperature of 25°C and shaking in 500 ml baffled flasks were maintained for 14 h. The cells were harvested by centrifugation for 10 min at room temperature (5000*g*). The pellet was resuspended in lysis buffer (200 m*M* sodium chloride, 20 m*M* sodium phosphate, 20 m*M* imidazole, Pefabloc SC protease inhibitor cocktail, pH 6.3) and sonicated three times for 25 s on ice (output control 5, duty cycle 70, Branson Ultrasonics). Cell debris was removed by centrifugation (20 min, 20 000*g*, 25°C). Protein purification was then performed at room temperature using buffers precooled to 4°C. The supernatant was loaded onto an Ni–NTA column (Quiagen, 5 ml). The column was washed with nine column volumes (CV) of wash buffer [200 m*M* sodium chloride, 20 m*M* sodium phosphate, 20 m*M* imidazole, 10%(*v*/*v*) glycerol, pH 6.3], 9 CV low-salt washing buffer [20 m*M* sodium chloride, 20 m*M* sodium phosphate, 20 m*M* imidazole, 10%(*v*/*v*) glycerol, pH 6.3], 9 CV high-salt washing buffer [1 *M* sodium chloride, 20 m*M* sodium phosphate, 20 m*M* imidazole, 10%(*v*/*v*) glycerol, pH 6.3] and finally 9 CV wash buffer. The protein was eluted with 4.5 CV elution buffer [200 m*M* sodium chloride, 20 m*M* sodium phosphate, 250 m*M* imidazole, 10%(*v*/*v*) glycerol, pH 6.3].

The eluate was directly loaded onto a DARPin R7 affinity column that specifically recognizes the N-terminal sfGFP tag (DARPin R7 coupled to Sepharose, 3 ml; Supplementary Section S2; Hansen *et al.*, 2017). The resin was washed with 15 CV wash buffer containing 200 m*M* sodium chloride, 15 CV wash buffer containing 20 m*M* sodium chloride, 15 CV wash buffer containing 1 *M* sodium chloride and finally 15 CV crystallization buffer (200 m*M* sodium chloride, 20 m*M* sodium phosphate, pH 6.3). The EngBF-DARPin fusion protein was eluted in batch mode: after adding 2 ml crystallization buffer containing 1 mg HRV C3 protease, the mixture was incubated for 3 h at room temperature with gentle agitation. The resin was washed with 10 ml crystallization buffer. The supernatant and the washing solution were combined and applied onto an Ni–NTA column (Qiagen, 2 ml) to remove the cleaved His_6 tag and the HRV C3 protease. The purified proteins were directly used for crystallization.

2.5. Characterization by surface plasmon resonance

Affinities were calculated from kinetic parameters that were measured by surface plasmon resonance on a ProteOn XPR36 instrument equipped with a NeutrAvidin-containing NLC chip (Bio-Rad) in PBS supplemented with 0.005% Tween 20. Two ligand channels were coated with 30 n*M* ZHAWOC8403 for 170 s (70 response units). Unfused DARPins or EngBF-DARPin fusions were injected at flow rates of 60 µl min^{-1} for 360 s followed by a dissociation phase of 1800 s. Between measurements the chip was regenerated with 1.5 m*M* glycine–HCl pH 2.5. Data were processed using the *ProteOn Manager* software (version 3.1.0.6). The processed sensogram data were imported into the *BIAevaluation* software (version 4.1) and fitted using the Langmuir model. In cases where the sensogram data clearly deviated from the expected 1:1 binding model, the data were fitted to the heterogenous ligand and two-step binding models. Since the heterogeneous ligand model revealed better fitting values, we selected this model if the Langmuir model was not applicable.

2.6. Structure determination

EngBF_L1_DARPin fusion proteins were concentrated to 10–20 mg ml^{-1} using Amicon Ultra-4 centrifugal concentrators (50 kDa molecular-weight cutoff, Merck Millipore). A 10 m*M* stock solution of ZHAWOC6027 was prepared in DMSO. 50 µl protein solution was mixed with 15 µl ZHAWOC6027 stock solution (approximately a 20-fold to 40-fold molar excess) and incubated on ice for 1 h. The protein–peptide mixture was set up for crystallization in sitting-drop vapor-diffusion experiments in 96-well plates. Crystallization conditions were screened around the established conditions for EngBF crystals [25% 2-methyl-2,4-pentanediol (MPD), 3% PEG 20 000, 0.2 *M* sodium chloride, 0.01 *M* manganese chloride, 0.1 *M* MES–NaOH pH 6.9] (Suzuki *et al.*, 2009), changing the pH along the columns (from pH 6 to 7) and the MPD:PEG 20 000 ratio along the rows [MPD from 23%(*v*/*v*) to 27%(*v*/*v*) and PEG 20 000 from 5%(*v*/*v*) to 2%(*w*/*v*)]. Three different ratios of reservoir:protein solution (1:1, 2:1 and 3:1) in 300–400 nl drops were used per well and were incubated against 75 µl reservoir solution at 4°C. Crystals of the EngBF_L1_E4_v1, EngBF_L1_E4_v2 and EngBF_L1_F11_v1 constructs grew within 25 days, whereas the EngBF_L1_F11_v2 construct did not crystallize under the expected conditions, even in the presence of seed crystals from another construct or in the absence of target peptide.

The crystals were mounted in cryo-loops from Hampton Research and flash-cooled in liquid nitrogen without any further cryoprotectant. X-ray diffraction data were collected at a wavelength of 1.0 Å on beamline X06SA at the Swiss Light Source, Paul Scherrer Institute (PSI), Villigen, Switzerland equipped with an EIGER 16M detector (Dectris, Baden-Wättwil, Switzerland). The data were processed with *XDS*, *AIMLESS* and *autoPROC* (Evans, 2011; Kabsch, 2010; Vonrhein *et al.*, 2011). To ensure unique assignment of the polar 6_5 screw axis and consistent allocation of test reflections, we used the EngBF_L1_G10 diffraction data as a reference data set (PDB entry 6qfk; Ernst *et al.*, 2019). Calculation of the electron density and refinement were performed using *BUSTER* version 2.10.4. The difference electron density was sharpened using the ligand-chasing option (`-L`) in *BUSTER*. Restraints for the ZHAWOC6027 peptide were calculated using the *Grade* server (Smart *et al.*, 2011). After an initial refinement round without peptide the difference electron density was sufficiently clear to position the ZHAWOC6027 molecule using *Rhofit* (Smart *et al.*, 2014). Refinement statistics are given in Table 1. For model building and preparation of figures we used *Coot* and *PyMOL* (DeLano, 2002; Emsley *et al.*, 2010). Real-space correlation values were calculated with *Phenix* (Liebschner *et al.*, 2019). Structures were deposited in the PDB with the accession numbers given in Table 1.

Table 1
Data-collection and refinement statistics.

Values in parentheses are for the highest resolution shell.

	EngBF_L1_E4_v1–ZHAWOC6027	EngBF_L1_F11_v1–ZHAWOC6027
PDB code	8a19	8a1a
Crystallization conditions	2.55% PEG 20 000, 26.72% MPD, 0.2 *M* NaCl, 0.01 *M* $MnCl_2$, 0.1 *M* MES–NaOH, pH 6.43	3.64% PEG 20 000, 24.82% MPD, 0.2 *M* NaCl, 0.01 *M* $MnCl_2$, 0.1 *M* MES–NaOH, pH 6.43
Data statistics		
Resolution range (Å)	98.94–2.36 (2.47–2.36)	166.161–2.05 (2.24–2.05)
Space group	$P6_5$	$P6_5$
a, *b*, *c* (Å)	192.76, 192.76, 122.83	191.87, 191.87, 122.41
α, β, γ (°)	90, 90, 120	90, 90, 120
Total reflections	1147539 (60193)	5229568 (250280)
Unique reflections	96740 (4841)	123411 (6170)
Multiplicity	11.9 (12.4)	42.4 (40.6)
Completeness (%)		
Spheroidal	90.6 (35.9)	76.6 (16.2)
Ellipsoidal	94.8 (51.0)	96.2 (70.8)
Mean $I/\sigma(I)$	8.8 (1.5)	13.9 (1.7)
Wilson *B* factor (Å^2)	42.24	38.67
ISA	20.09	23.71
R_{merge}†	0.227 (1.950)	0.290 (3.217)
R_{meas}†	0.237 (2.033)	0.294 (3.258)
$R_{p.i.m.}$†	0.069 (0.575)	0.045 (0.510)
$CC_{1/2}$	0.996 (0.599)	0.998 (0.698)
Refinement statistics		
Resolution range (Å)	34.52–2.36 (2.44–2.36)	49.28–2.05 (2.12–2.05)
Reflections used in refinement	96686 (3079)	123376 (772)
Reflections used for R_{free}	4853 (161)	6165 (37)
R_{work}	0.1550 (0.2443)	0.1539 (0.2456)
R_{free}	0.1831 (0.2755)	0.1761 (0.2490)
No. of atoms		
Total	11807	12109
Macromolecules	10419	10435
Ligands	137	136
Solvent	1251	1538
Protein residues	1345	1345
R.m.s.d., bond lengths (Å)	0.012	0.011
R.m.s.d., angles (°)	1.61	1.58
Ramachandran statistics		
Favoured (%)	96.35	96.72
Allowed (%)	3.57	3.13
Outliers (%)	0.07	0.15
Rotamer outliers (%)	1.99	2.34
Clashscore	1.94	1.74
Average *B* factors (Å^2)		
Overall	51.85	49.81
Macromolecules	50.94	48.08
EngBF	43.71	40.64
DARPin	102.97	101.49
Ligands	105.27	115.38
ZHAWOC6027	120.79	142.49
Solvent	53.55	55.75
Real-space correlation	0.91	0.92
ZHAWOC6027	0.78	0.63

† Calculated for all I^+ and I^- measurements together.

Raw diffraction data were uploaded to the Integrated Resource for Reproducibility in Macromolecular Crystallography (https://www.proteindiffraction.org).

3. Results

In order to display the target molecule ZHAWOC6027 in a unique orientation in the host lattice a selectively binding DARPin is required. Typically, targets for the selection of DARPins by ribosome display are immobilized using the tight interaction between biotin and NeutrAvidin. A biotin moiety was therefore coupled to the N-terminal benzoyl group of ZHAWOC6027 via an amide bond. The biotinylated compound ZHAWOC8403 harbors an 11-mer polyethylene glycol (PEG) linker to prevent steric hindrance between the peptide moiety and the nascent DARPin chain during ribosome display (Supplementary Fig. S1).

ZHAWOC8403 was immobilized to select binders from a DARPin library (Plückthun, 2012, 2015; Brauchle *et al.*, 2014) that encodes DARPins with three internal repeats (N3C) and a stabilized C-cap with and without randomized capping repeats (Kramer *et al.*, 2010; Schilling *et al.*, 2014). Initially, 32 clones were sequenced and 25 unique DARPins were identified. Just two of the 25 isolated hits belonged to the N3C lineage, whereas the remaining 23 hits contained only two internal repeats (N2C), which are present in small quantities due to the assembly process of the library from single-repeat building blocks. Finally, only two hits, designated E4 and F11, showed a clear signal in the high-throughput ELISA screen (Supplementary Fig. S2). DARPin E4 shows a higher signal compared with F11 and is clearly monomeric, which is not the case for F11 (data not shown).

DARPins E4 and F11 were fused to the C-terminus of EngBF using the rigid-helix fusion strategy (Wu *et al.*, 2017; Batyuk *et al.*, 2016). Two different fusion strategies, designated L1 and L2, have previously been developed (Ernst *et al.*, 2019). As ZHAWOC6027 is a relatively small target we used the L1 design, because L1 possesses lower *B* factors for the DARPin domain at the expense of less space for the target compared with L2. In both designs, an N3C DARPin is required to bridge the gap between symmetry-related molecules in the EngBF crystal lattice. Therefore, the N2C DARPin E4 and F11 sequences were grafted onto the EngBF_L1_G10 design, which is an N3C DARPin. Due to the repetitive architecture of DARPins two alternative alignment registers between the N2C DARPin E4 (or F11) and the N3C DARPin G10 are meaningful (constructs v1 and v2). Two fusion constructs between EngBF and DARPin E4 in the v1 or v2 alignment registers were thus

Table 2
Binding kinetics for ZHAWOC8403 determined by SPR.

n.d., not determined.

Construct	Kinetic model†	k_{on1} (M^{-1} s^{-1})	k_{off1} (s^{-1})	K_{d1} (M)	R_{max1}	k_{on2} (M^{-1} s^{-1})	k_{off2} (s^{-1})	K_{d2} (M)	R_{max2}	χ^2
DARPin E4	HL	1.15×10^5	4.39×10^{-4}	3.80×10^{-9}	29.9	2.06×10^6	1.09×10^{-2}	5.32×10^{-9}	44.6	4.94
DARPin F11	L	3.54×10^4	9.33×10^{-4}	2.64×10^{-8}						2.97
EngBF_L1_DARPin E4_v1	HL	1.56×10^4	4.45×10^{-4}	2.87×10^{-8}	9.6	7.32×10^4	1.13×10^{-2}	1.55×10^{-7}	16.3	2.87
EngBF_L1_DARPin E4_v2	No fit	n.d.	n.d.	n.d.						
EngBF_L1_DARPin F11_v1	No fit	n.d.	n.d.	9.61×10^{-6}						7.52
EngBF_L1_DARPin F11_v2	HL	5.27×10^4	4.49×10^{-4}	8.54×10^{-9}	59.9	7.50×10^4	4.01×10^{-3}	5.34×10^{-8}	73.4	1.95

† Data were fitted using the following models: HL, heterogenous ligand, L, Langmuir 1:1 model, as implemented in the *BIAevaluation* software

generated by transferring residues at randomized positions from E4 to EngBF_L1_G10 depending on the selected alignment register. Since side chains from the N-cap and C-cap can participate in target binding and were randomized in the DARPin library, some residues from the caps that line the DARPin paratope were also transferred. For DARPin F11 we applied the same strategy (Supplementary Fig. S3).

All four EngBF-DARPin fusion proteins were expressed in *E. coli* BL21 Gold cells. The purified constructs were analyzed by SPR (Table 2). The SPR analysis confirmed the observations made in the initial ELISA screen, namely that unfused DARPin E4 binds ZHAWOC8403 significantly better than DARPin F11. For DARPin E4, alignment register v1 was superior to alignment register v2, because EngBF_L1_E4_v1 binds ZHAWOC8403 with similar kinetic constants to unfused DARPin E4, whereas no binding was detected for EngBF_L1_E4_v2 (Supplementary Fig. S4). For DARPin F11 it was the opposite: EngBF_L1_F11_v1 shows equally poor binding characteristics to DARPin F11, whereas alignment register v2 showed clearly improved binding for EngBF_L1_F11_v2.

Crystallization of all four EngBF-DARPin fusions in complex with ZHAWOC6027 was tested under the established conditions for EngBF (Ernst *et al.*, 2019; Suzuki *et al.*, 2009). All fusions except for EngBF_L1_F11_v2 crystallized at very similar MPD concentrations and in the same pH range. No attempts were made to establish new crystallization conditions for EngBF_L1_F11_v2. Crystals of EngBF_L1_E4_v1, EngBF_L1_E4_v2 and EngBF_L1_F11_v1 in complex with ZHAWOC6027 were analyzed on beamline X06SA at the Swiss Light Source (SLS) and diffracted to 2.36, 2.08 and 2.05 Å resolution, respectively. The unit-cell parameters deviated less than 0.6% from the unit-cell parameters of deposited EngBF constructs (Table 1), confirming that the crystal lattices are isomorphic. Difference Fourier analysis between the observed diffraction data and the isomorphic EngBF_L1_G10 structure (PDB entry 6qfk; Ernst *et al.*, 2019) without bound peptide showed clear difference electron density for ZHAWOC6027 at the expected position in EngBF_L1_E4_v1, weaker density in EngBF_L1_F11_v1 and no density in EngBF_L1_E4_v2 (Figs. 3*a*–3*c*). Therefore, refinement of the EngBF_L1_E4_v2 structure was abandoned. Initially, the peptide was fitted into the weaker difference electron density of EngBF_L1_F11_v1. The conformation of the peptide was confirmed later when the data for EngBF_L1_E4_v1–ZHAWOC6027 became available. For EngBF_L1_E4_v1–ZHAWOC6027 all residues from the peptide except the C-terminal βAla9 and Acba are resolved in the final electron-density map, whereas EngBF_L1_F11_v1–ZHAWOC6027 only shows density for residues CyHex2–Leu6 (Figs. 3*d* and 3*e*). Refinement of the occupancies for ZHAWOC6027 in complex with EngBF_L1_E4_v1 and EngBF_L1_F11_v1 converged to 0.92 and 0.89, respectively. Thus, the relatively poor density is a consequence of the elevated *B* factor and is not due to low occupancy of the target molecule. The *B* factor increases constantly from the N- to the C-terminus of the host lattice (Figs. 2*b* and 2*c*). The average *B* factors for the EngBF, DARPin and target moieties in EngBF_L1_E4_v1–ZHAWOC6027 are 43.71, 102.97 and 120.79 Å^2, respectively (Table 1).

In the EngBF_L1_E4_v1–ZHAWOC6027 complex, peptide residues CyHex2–Aib8 adopt a distorted α-helical conformation with canonical hydrogen bonds Leu3 O···Aib7 N (2.9 Å), Aib4 O···Aib8 N (3.5 Å) and Leu5 O···βAla9 N (3.5 Å). The distance between CyHex2 O and Leu6 N (4.2 Å) is too long for a hydrogen bond. Despite the weak electron density this conformation is also seen in the EngBF_L1_F11_v1 complex (Fig. 4*a*). ZHAWOC6027 binds to EngBF_L1_E4_v1 in a parallel orientation. Upon binding a surface area of 612 Å^2 is buried at the interface, accounting for 46% of the molecular surface of ZHAWOC6027 (Supplementary Fig. S5). The E4 paratope is dominated by hydrophobic amino acids, because ZHAWOC6027 also comprises only hydrophobic residues. However, the ZHAWOC6027 main chain participates in hydrogen bonds; for example, the ZHAWOC6027 helix dipole moment is compensated by polar residues from EngBF_L1_E4_v1. The Gln1559 and Arg1634 side chains form hydrogen bonds to the N- and C-termini of ZHAWOC6027, respectively (Gln1559 NE2···Pro1 O, 3.1 Å; Gln1559 OE1···Leu N, 3.0 Å; Arg1634 NH2···Leu6 O, 3.6 Å; Arg1634 NE···Aib7 O, 3.0 Å; Fig. 4*b*). Furthermore, the ZHAWOC6027 main chain interacts via water-mediated hydrogen bonds with the Asp1621 side chain (Asp1621 OD2···Wat914···Wat915···Aib4 O).

Hydrophobic contacts occur between the Fben group at the N-terminus of ZHAWOC6027, which rests against Trp1534 and forms π-stacking interactions with the indole ring (for example Trp1534 CG···Fben C1, 3.6 Å). The Leu3 side chain fits into a hydrophobic pocket formed by the side chains of Leu1564, Phe1567 and Leu1597 (Phe1567 CD2···Leu3 CD2,

3.6 Å; Leu1564 CD2···Leu3 CD1, 3.8 Å; Leu1567 CD2···Leu3 CB, 3.8 Å) and the Aib7 side chain interacts with the side chains of Phe1567, Ala1600 and Leu1601 from EngBF_L1_E4_v1 (Phe1567 CE1···Aib7 CB1, 3.7 Å; Ala1600-CB···Aib7 CB2, 3.7 Å; Leu1601 CD2···Aib7 CB1, 3.7 Å; Fig. 4*c*). Since only half of the hydrophobic ZHAWOC602 surface is covered by the DARPin paratope, some hydrophobic side chains, such as Pro1, Leu5 and Leu6, are solvent-exposed. The hydrophobic CyHex2, Aib4 and Aib8 side chains are partially solvent-exposed and interact with residues from the DARPin β-hairpins. The CyHex2 side chain is sandwiched between Tyr1557 and Thr1590 (Tyr1557 CG···CyHex2 CG, 3.5 Å; Thr1590 CG2···CyHex2 CE1, 3.6 Å). Aib4 interacts with Thr1590 and Thr1592 (Thr1590 OG1···Aib4 CB2, 3.5 Å; Thr1592 OG1···Aib4 CB1, 3.4 Å) and Aib8 with Leu1630 (Leu1630 CD2···Aib8 CB1, 3.9 Å). To allow the polar hydroxyl groups from Thr1590 and Thr1592 to participate in hydrophobic contacts they form an intramolecular hydrogen bond (Thr1590 OG1···Thr1592 OG1, 2.9 Å).

ZHAWOC6027 is mainly recognized by residues from the first and second internal repeats of EngBF_L1_E4_v1, which have been grafted from the parental DARPin E4 in the v1 alignment register (Supplementary Fig. S3). Only Asp1621, Leu1630 and Arg1634 belong to the third internal repeat. Asp1621 and Leu1630 are invariant in the DARPin framework and Arg1634 was grafted from the DARPin E4 C-cap.

Bound ZHAWOC6027 shows a similar structure to those of leucinostatin A (CCDC entry 1183178; Cerrini *et al.*, 1989) and helioferin A (PDB entry 6evh; Gessmann *et al.*, 2018), which were obtained by crystallizing the free peptides from organic solvents. Residues Leu3–Aib8 in particular adopt the same α-helical conformation in all three structures (Fig. 4*d*). Differences exist at the termini, however: at the N-terminus of ZHAWOC6027 CyHex2 has rotated by approximately 180° around the CyHex2 C^{α}—C bond. We tried to model ZHAWOC6027 in the conformation seen in leucinostatin A, but placing the bulky Fben-Pro1 moiety into the CyHex2 side-chain density causes strong difference electron density around CyHex2, suggesting that the current assignment is correct. At the C-terminus of leucinostatin A, βAla9 and DPDA adopt a 3_{10}-helix conformation, whereas in EngBF_L1_E4_v1–

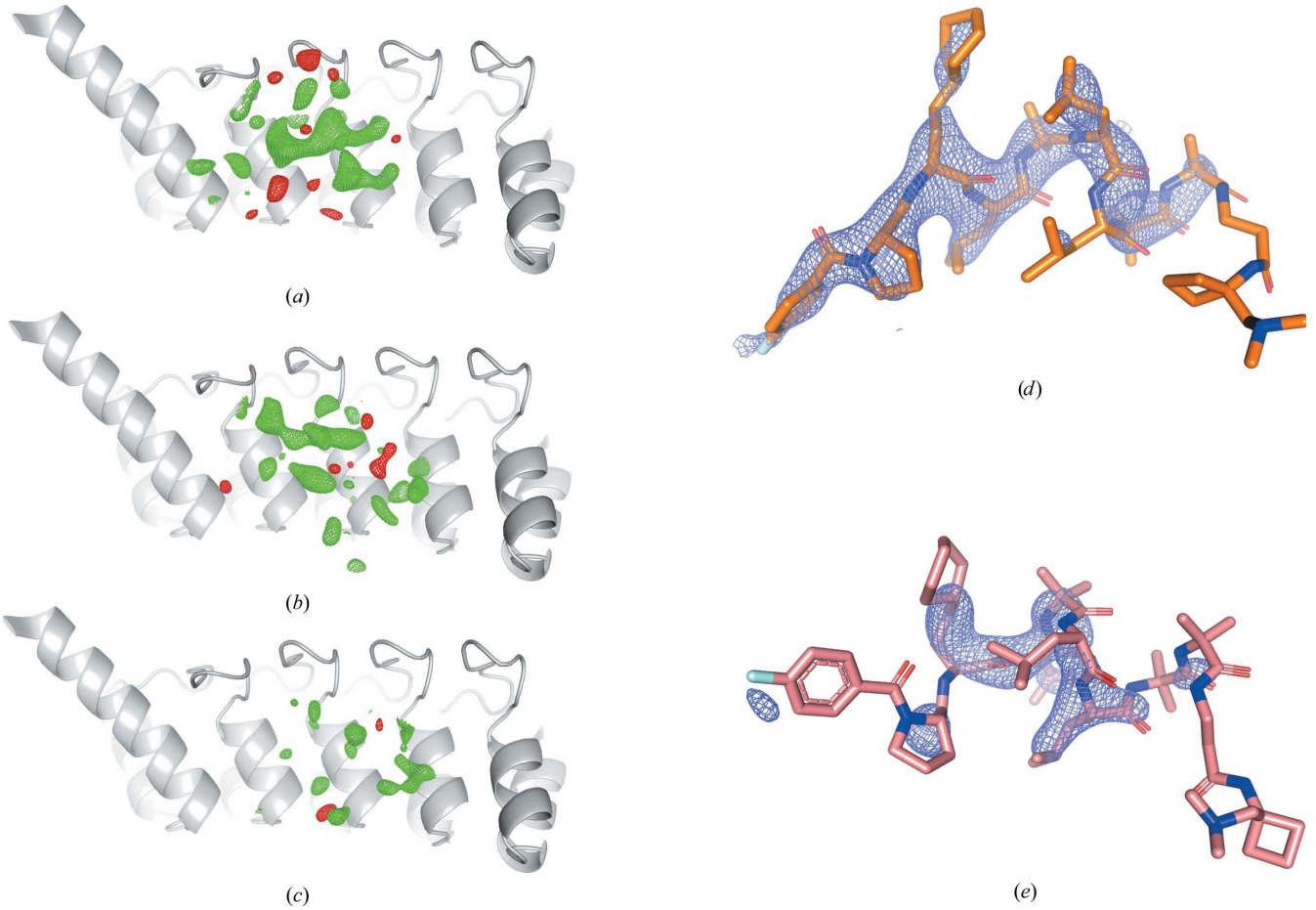

Figure 3
Electron-density maps for ZHAWOC6027 bound to the DARPin paratope. The difference electron-density maps without sharpening are shown in red and green at contour levels of -4σ and $+4\sigma$, respectively, for (*a*) EngBF_L1_E4_v1, (*b*) EngBF_L1_F11_v1 and (*c*) EngBF_L1_E4_v2. The final σ_A-weighted $2F_o - F_c$ maps were contoured at 1σ and are shown in blue for (*d*) EngBF_L1_E4_v1 and (*e*) EngBF_L1_F11_v1. Residues 1517–1680 of the EngBF-DARPin fusion are shown as a gray cartoon with the N-terminus at the top left.

ZHAWOC6027 βAla9 and Acba are disordered, probably because the Arg1634 side chain from EngBF_L1_E4_v1 occupies the βAla9 position.

4. Discussion

The crystal structures of isolated hydrophobic peptides such as leucinostatin A and helioferin A revealed completely helical conformations, with seven canonical hydrogen bonds involving all residues of the peptides. For ZHAWOC6027 a similar three-dimensional structure was assigned based on NOE NMR data recorded in deuterated methanol (Brand *et al.*, 2021). Since it has been known for a long time that organic solvents, for example trifluorethanol, can induce the formation of helices in natively unstructured peptides (Goodman & Listowsky, 1962; Jasanoff & Fersht, 1994; Luo & Baldwin, 1997) the question arises: what kind of structure does a poorly soluble hydrophobic peptide adopt under native-like conditions? To answer this question for the ZHAWOC6027 peptide, we applied host lattice display technology (Ernst *et al.*, 2019). We selected two DARPins that recognize ZHAWOC6027 with high affinity, and thus at low concentration, in PBS. The DARPin library predominantly encodes DARPins with three internal repeats. However, DARPins with just two internal repeats were selected because shorter variants are preferred during the PCR amplification step, and in the present case the third internal repeat does not improve the affinity for ZHAWOC6027 to compensate for this disadvantage.

DARPin E4 binds ZHAWOC6027 with nanomolar affinity, but the SPR data do not follow the expected 1:1 binding model (Table 2). Instead, either a heterogenous ligand-binding or a two-step binding model (data not shown) were required to

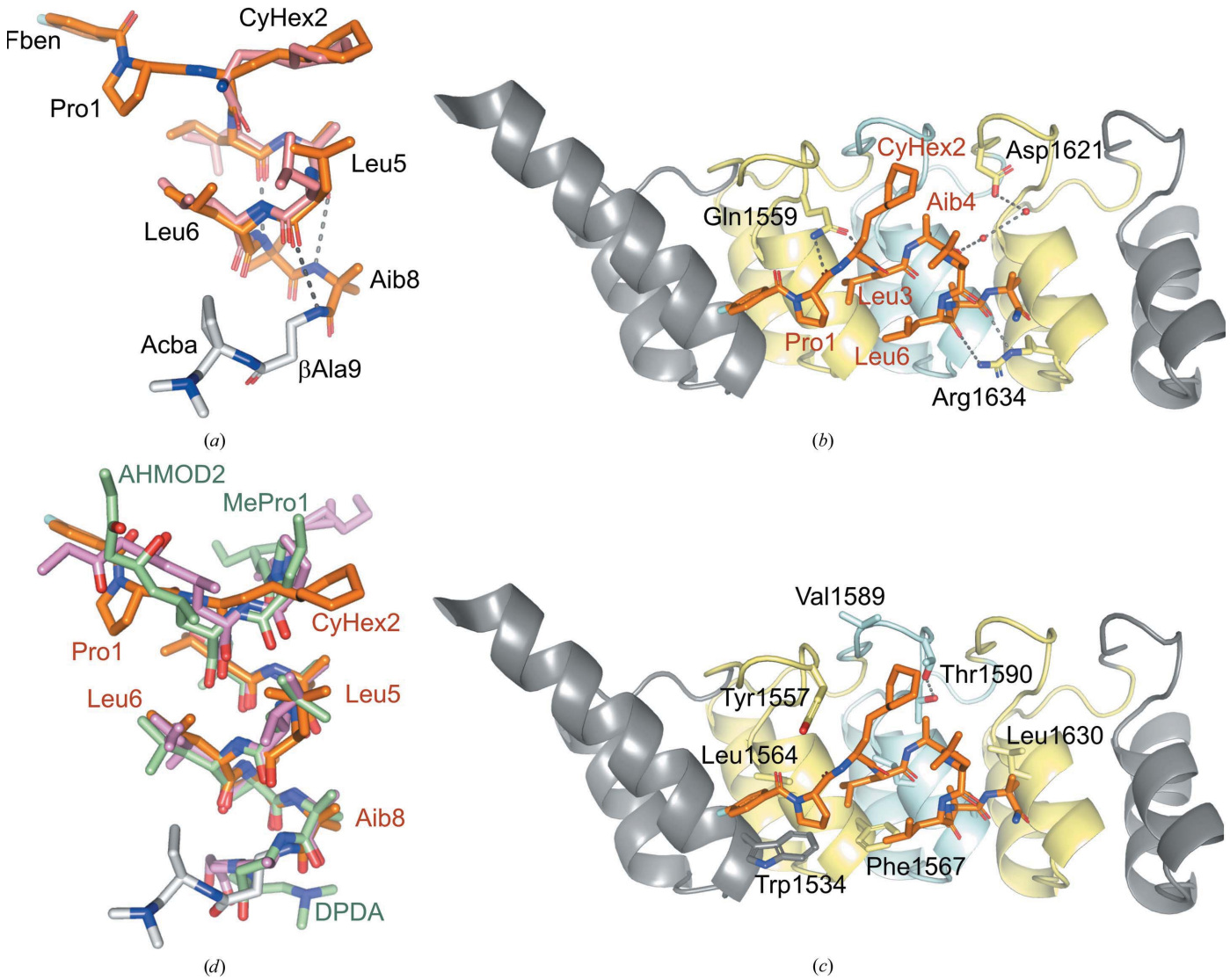

Figure 4
Recognition of ZHAWOC6027 by EngBF_L1_E4_v1. Hydrogen bonds are shown as dashed lines in gray. (*a*) Superposition of ZHAWOC6027 bound to EngBF_L1_E4_v1 (orange C atoms) and EngBF_L1_F11_v1 (wheat C atoms). The βAla9-Acba moiety is shown with white C atoms because it is not defined in the electron-density map. Polar (*b*) and hydrophobic (*c*) interactions at the ZHAWOC6027 binding site. DARPin E4 repeats are colored as in Supplementary Fig. S3. Residues belonging to ZHAWOC6027 are labeled in orange. (*d*) Superposition of leucinostatin A (green C atoms) and helioferin A (pink C atoms) on ZHAWOC6027 (orange C atoms). Residues from leucinostatin A are labeled in green.

interpret the sensorgram data (Supplementary Fig. S4). Considering the flexibility of the N- and C-termini of ZHAWOC6027 (Fig. 4*a*), a binding model in which the immobilized ligand adopts different conformations is conceivable and has been observed previously for other short antimicrobial peptides such as melittin (Hall & Aguilar, 2010).

Interestingly, grafting of the N2C DARPin E4 onto the N3C EngBF_L1_G10 was only successful in one of the two registers. The EngBF_L1_E4_v1 fusion protein shows similar k_{off} rates compared with unfused DARPin E4, whereas the association rate constants (k_{on}) are one order of magnitude lower (Table 2). Unexpectedly, alignment register v2 abrogated binding completely. Hence, no difference electron density for the ligand was observed (Fig. 3*c*). The lack of affinity could be caused by steric clashes between the ligand and the EngBF_L1 framework residues in the v2 register. The EngBF_L1_E4_v1–ZHAWOC6027 structure reveals that the N-terminal fluorobenzoyl group would bind close to the N-terminus of the parental DARPin E4 (Supplementary Fig. S6). In the v1 register there is sufficient space for the fluorobenzoyl group because the N-terminal helix is straight, but in the v2 register the fluorobenozyl group would clash with the Glu1559 side chain from the preceding framework repeat.

DARPin F11 shows a lower affinity for ZHAWOC6027 compared with E4, as had already been seen in the initial high-throughput ELISA and was subsequently confirmed by SPR (Supplementary Figs. S2 and S4, Table 2). Grafting of F11 in alignment register v1 decreased the affinity even further. The weak difference electron density in EngBF_L1_F11_v1 thus does not come as a surprise, considering the lower occupancy due to the poorer binding affinity. Interestingly, the alternative v2 register significantly improved the affinity, but the complex no longer crystallizes under the established conditions. Both observations support the hypothesis that grafting of F11 in alignment register v2 could have altered the overall structure of the DARPin. Even gentle bending of the DARPin superhelix would prevent EngBF_L1_F11_v2 from adopting the expected crystal lattice and it could improve the DARPin paratope with the consequence of a superior binding affinity.

ZHAWOC6027 shows similar conformations in EngBF_L1_E4_v1 and EngBF_L1_F11_v1 (Fig. 4*a*) because both DARPins possess similar residues at the randomized positions (Supplementary Fig. S3) and many hydrophobic residues are even identical, as shown in Fig. 4(*c*). Differences occur at the ZHAWOC6027 termini. Gln1559 and Arg1634 from E4, which recognize the N- and C-termini of ZHAWOC6027, respectively, are replaced by Thr1559 and Trp1634 in F11. Additionally, E4 residues Thr1590 and Thr1592, which contact the hydrophobic Aib4 of ZHAWOC6027, are replaced by Leu1590 and Asp1592 in F11. Surprisingly, hydrophilic residues, such as Thr and Asp, occur at position 1592, despite the hydrophobicity of the ligand. In both cases the side chain at position 1592 forms hydrogen bonds, either to Thr1590 in E4 or to the framework residue Asp1621 in F11.

Both structures confirm that ZHAWOC6027, and perhaps other leucinostatin derivatives as well, can adopt conformations which are less compact than the chiefly α-helical conformations seen in the crystal structures of free leucinostatin A and helioferin or in the NMR structure of free ZHAWOC6027 (Cerrini *et al.*, 1989; Gessmann *et al.*, 2018; Brand *et al.*, 2021). The free structures were obtained from highly concentrated samples analyzed in organic solvents, which support the formation of intramolecular hydrogen bonds (Goodman & Listowsky, 1962; Jasanoff & Fersht, 1994; Luo & Baldwin, 1997). The complex structures presented above have been crystallized from MPD, which could also induce α-helical conformations. However, DARPins E4 and F11 were selected in PBS and in the absence of MPD. If the crystallization conditions could significantly alter the conformation of ZHAWOC6027 we would expect empty binding sites.

The structure of ZHAWOC6027 obtained by host lattice display suggests that the termini are flexible under aqueous conditions. The common feature of the free and complexed structures is the α-helical conformation of Leu3–Aib8 (Fig. 4*d*). This fragment contains three Aib residues. Due to the bulky methyl group that replaces the C^{α} proton in alanine, Aib is a stronger inducer of 3_{10}- and α-helices than any other proteinogenic amino acid (Schweitzer-Stenner *et al.*, 2007). In particular, the N-terminus shows a transition from a α-helical conformation with an (n to n + 4) hydrogen-bond pattern towards a 3_{10}-helix with an (n to n + 3) hydrogen-bond pattern because the distance between CyHex2 O and Leu5 N (4.1 Å) is shorter than the distance between CyHex2 O and Leu6 N (4.2 Å). Similar structural transitions from 3_{10}- to α-helical conformations are seen in other Aib-rich peptides such as efrapeptidin (Supplementary Fig. S7).

The structural mobility of the N-terminus of ZHAWOC6027 might be functionally important because it has been shown that the N-terminal residues HyLeu3 and Leu5 in particular are crucial for the antiproliferative activity of leucinostatin derivatives in cellular assays (Abe *et al.*, 2018). Unfortunately, the molecular target of the cytotoxic activity of leucinostatin A is not precisely known. It has been suggested that leucinostatin A and certain derivatives may either act as ionophores of the inner mitochondrial membrane (Brand *et al.*, 2021; Csermely *et al.*, 1994; Fresta *et al.*, 2000) or target the F_1F_o-ATP synthase (Shima *et al.*, 1990). It is possible that the structural flexibility of ZHAWOC6027 that is seen in the EngBF_L1_E4_v1 construct resembles the structural adaptation of ZHAWOC6027 to a complex binding site that requires partial restructuring of the α-helix conformation. Provided that ZHAWOC6027 is flexible at the termini in aqueous solution, binding to the DARPin paratope will also have an impact on its conformation. However, the selection of a suitable binder can only be successful for a conformation that is sufficiently populated and remains present in the aliquots that are used on different days in the different selection rounds. Under these conditions, DARPins can be picked from the library that are compatible with a defined solution structure of ZHAWOC6027. If ZHAWOC6027 were intrinsically unstructured and disordered in aqueous solution, we would expect the free and complexed structures to substantially differ from each other. Since this is not the case, we assume

that ZHAWOC6027 possesses a rather stable helical conformation with elevated flexibility of the termini under aqueous conditions.

5. Related literature

The following references are cited in the supporting information for this article: Abrahams *et al.* (1996); Kim *et al.* (2015).

Acknowledgements

We would like to thank the following people for skillful technical support: Thomas Reinberg and Sven Furler for the high-throughput DARPin selection experiments, Tong Chen and Loan Nguyen for cloning and sequencing, Gabriela Nagy-Davidescu for SPR experiments, Jens Sobek from the Functional Genomics Center Zürich for discussing the SPR analysis, Beat Blattmann from the high-throughput crystallization center at the University of Zürich and the staff of beamlines X06SA and X06DA at the Swiss Light Source, PSI, Villigen, Switzerland for supporting diffraction data collection. Conflict of interest statement: M. Adams is currently CEO of Bacoba AG, who supported this research financially and logistically.

Funding information

This project was supported by grant F-41105-23-01 from the Stiftung für wissenschaftliche Forschung, University of Zürich to PREM and by grant CTI 19208.1 PFLS-LS from the Swiss Commission for Technology and Innovation as well as direct financial contributions from Bacoba AG, Basel to RR.

References

Abrahams, J. P., Buchanan, S. K., Van Raaij, M. J., Fearnley, I. M., Leslie, A. G. & Walker, J. E. (1996). *Proc. Natl Acad. Sci. USA*, **93**, 9420–9424.

Abe, H., Kawada, M., Sakashita, C., Watanabe, T. & Shibasaki, M. (2018). *Tetrahedron*, **74**, 5129–5137.

Arai, T., Mikami, Y., Fukushima, K., Utsumi, T. & Yazawa, K. (1973). *J. Antibiot.* **26**, 157–161.

Batyuk, A., Wu, Y., Honegger, A., Heberling, M. M. & Plückthun, A. (2016). *J. Mol. Biol.* **428**, 1574–1588.

Brand, M., Wang, L., Agnello, S., Gazzola, S., Gall, F. M., Raguž, L., Kaiser, M., Schmidt, R. S., Ritschl, A., Jelk, J., Hemphill, A., Mäser, P., Bütikofer, P., Adams, M. & Riedl, R. (2021). *Angew. Chem. Int. Ed.* **60**, 15613–15621.

Brauchle, M., Hansen, S., Caussinus, E., Lenard, A., Ochoa-Espinosa, A., Scholz, O., Sprecher, S. G., Plückthun, A. & Affolter, M. (2014). *Biol. Open*, **3**, 1252–1261.

Cerrini, S., Lamba, D., Scatturin, A., Rossi, C. & Ughetto, G. (1989). *Biopolymers*, **28**, 409–420.

Csermely, P., Radics, L., Rossi, C., Szamel, M., Ricci, M., Mihály, K. & Somogyi, J. (1994). *Biochim. Biophys. Acta*, **1221**, 125–132.

DeLano, W. L. (2002). *PyMOL*. http://www.pymol.org.

Dreier, B. & Plückthun, A. (2012). *Methods Mol. Biol.* **805**, 261–286.

Emsley, P., Lohkamp, B., Scott, W. G. & Cowtan, K. (2010). *Acta Cryst.* D**66**, 486–501.

Ernst, P., Plückthun, A. & Mittl, P. R. E. (2019). *Sci. Rep.* **9**, 15199.

Evans, P. R. (2011). *Acta Cryst.* D**67**, 282–292.

Fresta, M., Ricci, M., Rossi, C., Furneri, P. M. & Puglisi, G. (2000). *J. Colloid Interface Sci.* **226**, 222–230.

Fujita, D., Suzuki, K., Sato, S., Yagi-Utsumi, M., Yamaguchi, Y., Mizuno, N., Kumasaka, T., Takata, M., Noda, M., Uchiyama, S., Kato, K. & Fujita, M. (2012). *Nat. Commun.* **3**, 1093.

Fukushima, K., Arai, T., Mori, Y., Tsuboi, M. & Suzuki, M. (1983). *J. Antibiot.* **36**, 1613–1630.

Gessmann, R., Brückner, H., Berg, A. & Petratos, K. (2018). *Acta Cryst.* D**74**, 315–320.

Goodman, M. & Listowsky, I. (1962). *J. Am. Chem. Soc.* **84**, 3770–3771.

Hall, K. & Aguilar, M.-I. (2010). *Methods Mol. Biol.* **627**, 213–223.

Hansen, S., Stüber, J. C., Ernst, P., Koch, A., Bojar, D., Batyuk, A. & Plückthun, A. (2017). *Sci. Rep.* **7**, 16292.

Hashimoto, T., Ye, Y., Ui, M., Ogawa, T., Matsui, T. & Tanaka, Y. (2019). *Biochem. Biophys. Res. Commun.* **514**, 31–36.

Huber, T. R., McPherson, E. C., Keating, C. E. & Snow, C. D. (2018). *Bioconjug. Chem.* **29**, 17–22.

Inokuma, Y., Yoshioka, S., Ariyoshi, J., Arai, T., Hitora, Y., Takada, K., Matsunaga, S., Rissanen, K. & Fujita, M. (2013). *Nature*, **495**, 461–466.

Jasanoff, A. & Fersht, A. R. (1994). *Biochemistry*, **33**, 2129–2135.

Kabsch, W. (2010). *Acta Cryst.* D**66**, 125–132.

Kim, M. H., Woo, S. K., Kim, K. I., Lee, T. S., Kim, C. W., Kang, J. H., Kim, B. I., Lim, S. M., Lee, K. C. & Lee, Y. J. (2015). *ACS Med. Chem. Lett.* **6**, 528–530.

Kramer, M. A., Wetzel, S. K., Plückthun, A., Mittl, P. R. & Grütter, M. G. (2010). *J. Mol. Biol.* **404**, 381–391.

Lawson, D. M., Artymiuk, P. J., Yewdall, S. J., Smith, J. M., Livingstone, J. C., Treffry, A., Luzzago, A., Levi, S., Arosio, P., Cesareni, G., Thomas, C. D., Shaw, W. V. & Harrison, P. M. (1991). *Nature*, **349**, 541–544.

Liebschner, D., Afonine, P. V., Baker, M. L., Bunkóczi, G., Chen, V. B., Croll, T. I., Hintze, B., Hung, L.-W., Jain, S., McCoy, A. J., Moriarty, N. W., Oeffner, R. D., Poon, B. K., Prisant, M. G., Read, R. J., Richardson, J. S., Richardson, D. C., Sammito, M. D., Sobolev, O. V., Stockwell, D. H., Terwilliger, T. C., Urzhumtsev, A. G., Videau, L. L., Williams, C. J. & Adams, P. D. (2019). *Acta Cryst.* D**75**, 861–877.

Luo, P. & Baldwin, R. L. (1997). *Biochemistry*, **36**, 8413–8421.

Maita, N. (2018). *J. Am. Chem. Soc.* **140**, 13546–13549.

Mittl, P. R. E., Berry, A., Scrutton, N. S., Perham, R. N. & Schulz, G. E. (1994). *Acta Cryst.* D**50**, 228–231.

Mori, Y., Suzuki, M., Fukushima, K. & Arai, T. (1983). *J. Antibiot.* **36**, 1084–1086.

Otoguro, K., Ui, H., Ishiyama, A., Arai, N., Kobayashi, M., Takahashi, Y., Masuma, R., Shiomi, K., Yamada, H. & Omura, S. (2003). *J. Antibiot.* **56**, 322–324.

Plückthun, A. (2012). *Methods Mol. Biol.* **805**, 3–28.

Plückthun, A. (2015). *Annu. Rev. Pharmacol. Toxicol.* **55**, 489–511.

Radios, L., Kajtar-Peredy, M., Casinovi, C. G., Rossi, C., Ricci, M. & Tuttobello, L. (1987). *J. Antibiot.* **40**, 714–716.

Schilling, J., Schöppe, J. & Plückthun, A. (2014). *J. Mol. Biol.* **426**, 691–721.

Schweitzer-Stenner, R., Gonzales, W., Bourne, G. T., Feng, J. A. & Marshall, G. R. (2007). *J. Am. Chem. Soc.* **129**, 13095–13109.

Shima, A., Fukushima, K., Arai, T. & Terada, H. (1990). *Cell Struct. Funct.* **15**, 53–58.

Smart, O. S., Womack, T. O., Sharff, A., Flensburg, C., Keller, P., Paciorek, W., Vonrhein, C. & Bricogne, G. (2011). *Grade*, version 1.2.20. Global Phasing Ltd., Cambridge, UK.

Smart, O. S., Womack, T. O., Sharff, A., Flensburg, C., Keller, P., Paciorek, W., Vonrhein, C. & Bricogne, G. (2014). *Rhofit*, version 1.2.4. Global Phasing Ltd., Cambridge, UK.

Strobel, G. A., Torczynski, R. & Bollon, A. (1997). *Plant Sci.* **128**, 97–108.

Suzuki, R., Katayama, T., Kitaoka, M., Kumagai, H., Wakagi, T., Shoun, H., Ashida, H., Yamamoto, K. & Fushinobu, S. (2009). *J. Biochem.* **146**, 389–398.
Vonrhein, C., Flensburg, C., Keller, P., Sharff, A., Smart, O., Paciorek, W., Womack, T. & Bricogne, G. (2011). *Acta Cryst.* D**67**, 293–302.
Wang, G., Liu, Z., Lin, R., Li, E., Mao, Z., Ling, J., Yang, Y., Yin, W.-B. & Xie, B. (2016). *PLoS Pathog.* **12**, e1005685.
Ward, A. R. & Snow, C. D. (2020). *Curr. Opin. Struct. Biol.* **60**, 85–92.
Watanabe, T., Abe, H. & Shibasaki, M. (2021). *Chem. Rec.* **21**, 175–187.
Wu, Y., Batyuk, A., Honegger, A., Brandl, F., Mittl, P. R. E. & Plückthun, A. (2017). *Sci. Rep.* **7**, 11217.